Journal of
Materials Chemistry C

ROYAL SOCIETY
OF **CHEMISTRY**

PAPER

View Article Online
View Journal

Check for updates

Cite this: DOI: 10.1039/d6tc01061j

Carbon doping in GeTe drives differences in local structure and properties

John D. Langhout, †[a] Marisa D. Kelley, †[a] Danielle N. Alverson, [a] Laurence M. Barnes,[b] Celia Mercier,[c] Daniel Olds, [d] David P. Adams [e] and Megan M. Butala *[a]

Received 2nd April 2026,
Accepted 26th May 2026

DOI: 10.1039/d6tc01061j

rsc.li/materials-c

Advances in low-power, energy-efficient information storage and computing require understanding and controlling the atomic and nanoscale structures of functional materials, such as phase-change materials. Phase-change memory technology enables nonvolatile, low-power memory in devices by storing information through reversible changes in a phase-change material's atomic structure (*i.e.*, transformations between amorphous and crystalline phases) that have corresponding changes in properties, including electronic resistivity and optical reflectivity. Here, we apply complementary X-ray absorption spectroscopy and X-ray pair distribution function analyses to experimentally identify the local- and medium-range atomic structure differences of GeTe and C-doped GeTe thin films. Upon controlled heating, composition- and temperature-dependent atomic structure evolution in GeTe and C-doped GeTe films shows differences in bonding behavior and local structure that directly influence crystallization onset temperature. We find that the introduction of C interrupts Ge–Ge bonds in amorphous GeTe, altering the as-deposited structure to be more similar to the distorted rocksalt structure of crystalline α–GeTe. The change alters the response of the amorphous atomic structure to heating and also lowers the crystallization onset temperature, from 230 °C in GeTe to 220 °C in the C-doped film. The combined insights from both X-ray techniques provide understanding of structural transformations that enables the development and optimization of next-generation memory and computing materials.

1. Introduction

Phase-change memory (PCM) is a novel technology that provides a more scalable and energy-efficient alternative to existing non-volatile memory devices.[1–5] PCM relies on phase-change materials, which undergo changes in physical properties (and thus, digital states) upon fast and reversible phase transformations. These phase changes are controlled *via* resistive heating through a volume of phase-change material, the phase-change element, that reversibly amorphizes and crystallizes depending on the nature of the applied current pulse. In addition to the phase-change element, another crucial element of a PCM device is the 'selector', which enables the passing of high current through a single phase-change element with precision.[4,6]

Amorphous chalcogenides, such as GeTe, have been identified for use as a phase-change element as well as a selector element in PCM due to their phase change[7–16] and ovonic threshold switching (OTS) behavior, respectively.[17–19] OTS involves a volatile switch between a high and low resistivity state in response to an applied voltage.[4,20] This 'switching' occurs beyond a threshold voltage; when the applied voltage exceeds the threshold voltage, the selector allows current to pass through the selector and the phase-change material, inducing resistive heating and thus, a phase transformation in that specific element. Unlike the phase-change element, the ovonic material remains amorphous during operation.

Amorphized GeTe can recrystallize if held at a temperature below T_C for extended time.[8,14] Whether GeTe is used as a phase-change element or selector, increasing the stability of the amorphous phase (*i.e.*, raising the crystallization temperature, T_C) is of interest.[12,14,21] Stabilizing the amorphous phase increases the reliability of the memory device at elevated temperatures, such as during device processing or use in high-temperature and otherwise extreme environments. Unwanted crystallization of the selector device during processing or use

---

[a] *Department of Materials Science and Engineering, University of Florida, Gainesville, FL 32611, USA. E-mail: mbutala@ufl.edu*
[b] *Department of Chemical Engineering, University of Florida, Gainesville, FL 32611, USA*
[c] *Department of Electrical and Computer Engineering, University of Florida, Gainesville, FL 32611, USA*
[d] *National Synchrotron Light Source II, Brookhaven National Laboratory, Upton, NY 11973, USA*
[e] *Sandia National Laboratories, Albuquerque, NM 87185, USA*

† Equal contribution.

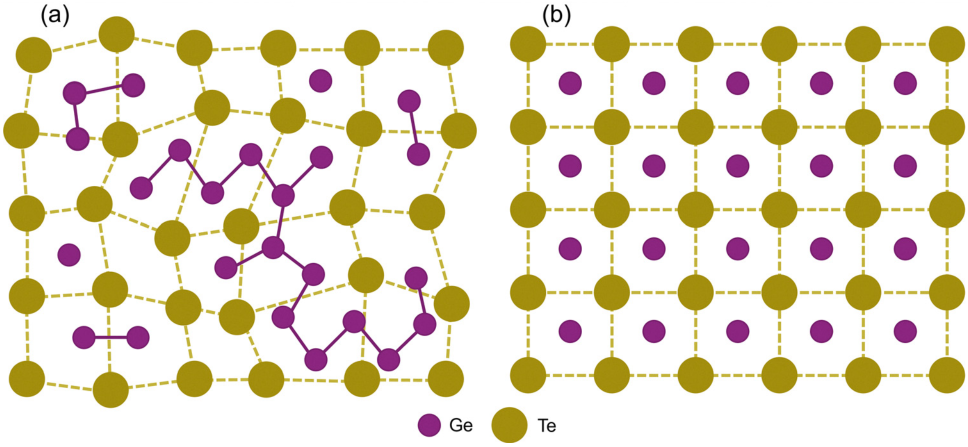

Fig. 1 Schematic of proposed GeTe model in the (a) amorphous and (b) crystalline states. Long Ge chains break apart with heating as the Te sublattice orders, finally reaching a distorted rocksalt structure with crystallization.

would be effectively impossible to reverse and diminish the lifetime and reliability of a device. Efforts to increase the stability of the amorphous phase of GeTe and similar chalcogenides typically involve doping with C and other elements.[4,12–14,18,21–24] Doping with C has been shown to improve the electronic properties and raise T_C of GeTe as a phase-change material[12–14] or selector.[18] In any case, the manner in which C incorporates into the amorphous structure of GeTe, and its effect on crystallization, must be better understood before it can be leveraged to design reliable and energy-efficient PCM devices.

Previous work indicates that the structure of amorphous GeTe is a highly disordered face-centered cubic (FCC) Te sublattice interspersed with chains of 2 or more Ge atoms (Fig. 1a).[8] This structure is dynamic with respect to temperature prior to crystallization. As the material heats, long Ge chains break and the atoms move toward their positions in the rhombohedral structure while the FCC-like Te sublattice gradually becomes more ordered.[8] Upon crystallization, the structure has a rhombohedral space group and resembles a distorted rocksalt structure (Fig. 1b).[8,13,25,26]

It is unknown how the presence of dopants, such as C, incorporate into this complex amorphous structure, and the mechanism by which these structural or chemical differences affect macroscopic properties (*e.g.*, crystallization temperature, resistivity). Here, we characterize phase-change and OTS materials GeTe and $(GeTe)_{0.96}C_{0.04}$ (C–GeTe). Both materials are deposited as amorphous thin films (300 nm) on fused silica substrates with thin (30 nm) TiN caps to prevent oxidation. C doping is expected to increase the stability of the amorphous phase because it raises the crystallization temperature,[14,21] but as we find here, this is not necessarily the case. When the films are held at elevated temperatures for an extended period of time, they are prone to crystallize below their T_C. Through *in situ* X-ray scattering and X-ray absorption spectroscopy (XAS) experiments during heating of the amorphous films, we find that C modifies the as-deposited amorphous structure of GeTe, which in turn modifies the response of the amorphous structure to heating, including the crystallization onset temperature.

2. Results and discussion

2.1. X-ray absorption spectroscopy

XAS data were collected from TiN-capped GeTe and C–GeTe films during *in situ* heating in air using a Linkam cell. The Ge K-edge spectra of amorphous films were recorded in 10 °C increments from room temperature through crystallization, with a 60 second dwell at each temperature before data were collected. Crystallization onset was evident by significant qualitative changes in X-ray absorption near-edge structure (XANES) spectra (Fig. 2). The GeTe film began to crystallize at 230 °C and the C–GeTe film began to crystallize at 220 °C. This decrease of crystallization onset temperature (the temperature at which local structure changes were first apparent) with the addition of C is in contrast to other studies on C-doped GeTe,[14,21] as well as the related phase-change material, $Ge_2Sb_2Te_5$, for which the temperature at which crystallization is complete increases with C content.[22,23,27]

Crystallization of GeTe depends on both time and temperature; GeTe can crystallize below its prescribed crystallization temperature if annealed for an extended period of time.[8,14] Indeed, XAS data were collected over a period of around 30 minutes (three ten-minute scans). Since T_C is defined as the temperature at which a film or device undergoes a rapid decrease in resistance, we use the term 'crystallization onset' to describe the onset of this observed structural change during extended heating, and note that crystallization onset temperature may be decoupled from actual crystallization temperature.

In a second set of *in situ* XAS measurements, *in situ* heating experiments were repeated with longer XAS scans to higher energies past the edge, appropriate for EXAFS analysis. These data were collected at larger temperature intervals (≈30 °C) at lower temperatures and narrow temperature intervals (10 °C) near the crystallization onset temperature identified in the first

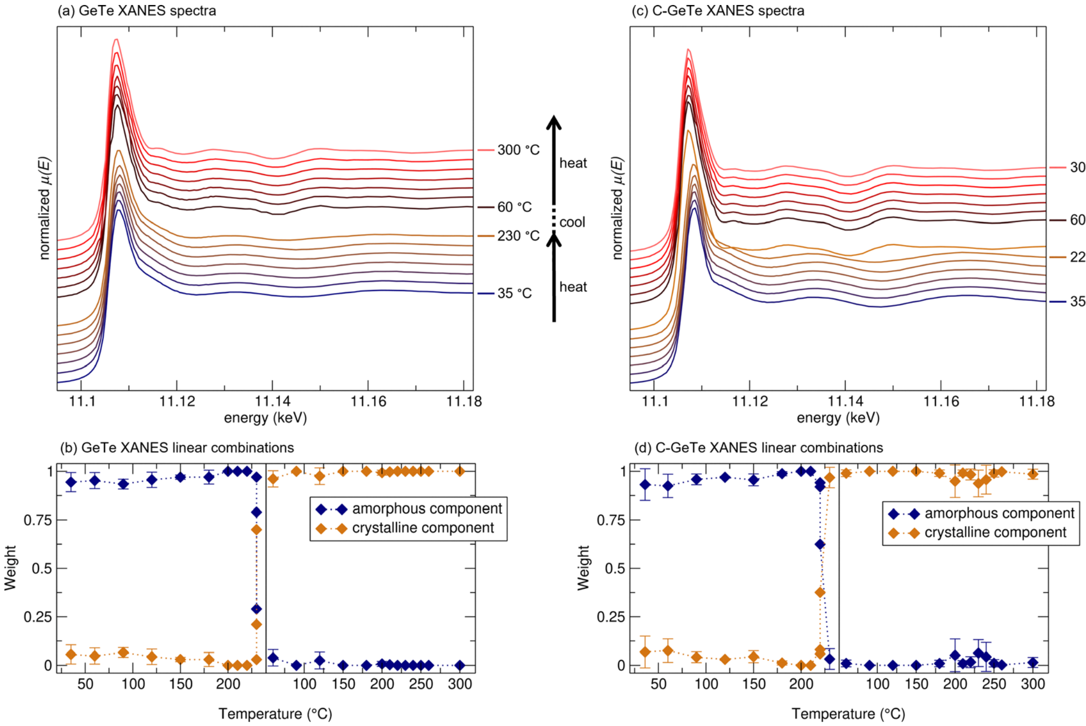

Fig. 2 Temperature-dependent XANES for select temperatures in (a) GeTe and (c) C–GeTe during two consecutive heating steps. Complete XANES datasets can be found in Fig. S1 and S2. The changes in spectra features at 230 °C for GeTe and 220 °C for C–GeTe correspond to the onset of crystallization. Linear combinations of amorphous and crystalline components were also fit to each XANES spectrum. Weights of each component, including error bars denoting one standard deviation from triplicate XANES measurements, are plotted for (b) GeTe and (d) C–GeTe to highlight the crystallization onset.

in situ XAS experiments. In addition, heating was completed in two stages to assess the degree of reversibility of local structure changes that might occur before crystallization; the first stage involved heating from room temperature to 230 °C, passive cooling to 60 °C, and a second heating stage through crystallization.

Crystallization is visibly incomplete at the crystallization onset temperatures, as evidenced by fitting a linear combination of crystalline and amorphous spectra to each XANES spectrum (Fig. 2b and d). For both films, the 'amorphous' component refers to the first XANES spectrum, collected at ambient temperature prior to heating, and the 'crystalline' component refers to the XANES spectrum collected at 120 °C upon the second heating, well after crystallization has occurred. Regardless, the phase changes of both GeTe and C–GeTe are complete upon intermediate cooling to 60 °C. In its application as a phase-change material, GeTe is brought to a temperature significantly above its crystallization temperature to achieve a rapid phase change.[11,12,14,28] When held near the crystallization onset temperature, however, the crystallization process is evidently more gradual, occurring over several minutes, which allows for a technique like XAS to capture the structure changes associated with crystallization.[8,10,29]

Fourier transformed (FT) extended X-ray absorption fine structure (FT-EXAFS) spectra were analyzed to better understand the local coordination environment of Ge in GeTe and C–GeTe films and their evolution in the amorphous state during heating. The FT-EXAFS spectra of GeTe and C–GeTe are visibly distinct, indicating a significant difference of the Ge environment in the two materials (Fig. 3).

Ge–C bonds are expected to be ≈2.05 Å in C–GeTe, as C preferentially bonds to Ge.[12] A small feature consistent with the Ge–C–Ge scattering path is present in the FT-EXAFS spectra for C–GeTe centered around 1.2 Å, indicating that C is bonding to Ge (Fig. S3). Yet, this signal is too low intensity (given the low scattering factor and low concentration of C) and too short to be quantitatively fit. Instead, the major differences in FT-EXAFS spectra shape are attributed to changes in the Ge–Ge and Ge–Te bonding environments driven by the presence of C. To better understand these coordination differences, structural models were fit to the FT-EXAFS data.

Models consisting of a first-shell single scattering Ge–Ge path and a first-shell single scattering Ge–Te path were fit to the amorphous FT-EXAFS data. The paths were calculated using a modified rhombohedral crystalline model of GeTe (spacegroup *R*3*m*)[26] in which Ge atoms are coordinated by six Te atoms in distorted edge-sharing octahedra with three long Ge–Te bonds and three short Ge–Te bonds. Ge–Te paths were calculated using the long Ge–Te bond. To generate Ge–Ge paths, the Te atoms comprising the shorter Ge–Te bonds surrounding the central Ge absorber were replaced with Ge atoms.

Both Ge–Ge and Ge–Te scattering paths were fit with their multiplicity (N), path length (R), and mean square relative displacement (σ^2) constrained to physical limits. Since both

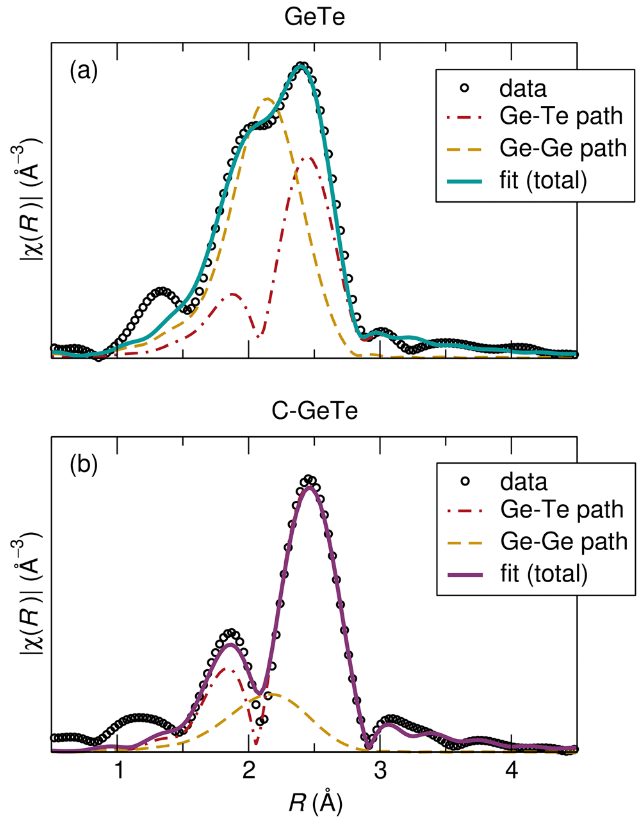

Fig. 3 Fits of the amorphous GeTe model to FT-EXAFS spectra of (a) GeTe and (b) C–GeTe at ambient temperature. Visible differences of features in $|\chi(R)|$ are reflected mostly by the relative intensities of the Ge–Te and Ge–Ge paths.

paths are first-shell single scattering paths, their multiplicity N is equivalent to the number of Ge or Te coordinating Ge. Likewise, the half-path length, R, is equivalent to the Ge–Ge or Ge–Te bond length, and the mean square relative displacement σ^2 is the bond length variance. Results of model fitting to FT-EXAFS spectra for GeTe and C–GeTe near room temperature (35 °C) are shown in Table 1 and Fig. 3.

The FT-EXAFS model fitting results highlight that C affects the Ge environment beyond simply the addition of Ge–C bonds (Fig. 3). In GeTe, the coordination of Ge by Ge and Te are nearly equal, both around 2. A Ge–Ge coordination of 2 is attributed to the bonding environment of Ge atoms in Ge chains, where most Ge atoms exist within a chain rather than isolated from other Ge atoms ($N_{\text{Ge–Ge}}$ of 0), in Ge_2 'dumbbells' ($N_{\text{Ge–Ge}}$ of 1), or at the termination of a chain ($N_{\text{Ge–Ge}}$ of 1).[6,8] In C–GeTe, each Ge is coordinated, on average, by 3 Te atoms and 1 Ge atom. This change can be interpreted as a shift in average Ge environment to more Ge_2 'dumbbell' configurations rather than long chains of bonded Ge atoms. This reflects how C likely incorporates into the amorphous structure: C prefers to covalently bond to Ge, replacing Ge–Ge bonds that otherwise connect to form Ge chains within the amorphous structure (Fig. 1a). Thus, C incorporation in amorphous C–GeTe disrupts Ge chains, resulting in an increase in isolated Ge atoms or Ge_2 dumbbell motifs.

Table 1 Results of fitting amorphous structural models to ambient temperature FT-EXAFS data for GeTe and C–GeTe. ± values refer to standard error derived in fitting[30]

GeTe

R-factor = 0.0146
S_0^2 = 0.79
ΔE_0 = 7.38 eV

Path	N	±	R (Å)	± (Å)	σ^2 (Å^2)	± (Å^2)
Ge–Ge	2.19	0.35	2.4772	0.0076	0.0055	0.0024
Ge–Te	1.81	0.35	2.6097	0.0141	0.0070	0.0039

C–GeTe

R-factor = 0.0026
S_0^2 = 0.79
ΔE_0 = 8.87 eV

Path	N	±	R (Å)	± (Å)	σ^2 (Å^2)	± (Å^2)
Ge–Ge	1.15	0.26	2.4950	0.0161	0.0091	0.0043
Ge–Te	2.85	0.26	2.6009	0.0065	0.0037	0.0012

The σ^2 values for the Ge–Ge and Ge–Te path also differ between the fit models. In GeTe, $\sigma_{\text{Ge–Ge}}^2$ is lower than $\sigma_{\text{Ge–Te}}^2$, indicating lower bond length variance, and higher bond rigidity. This is expected; the Ge–Ge bond is a shorter, homopolar covalent bond, and therefore stronger than the Ge–Te bond, which is longer and has more ionic character. Thus, the Ge–Ge bond length is less susceptible to static (*e.g.*, structural) and dynamic (*e.g.*, temperature-dependent) disorder. In contrast, in the C–GeTe fit, the value of $\sigma_{\text{Ge–Ge}}^2$ is higher, indicating a increased variance in Ge–Ge bond length and thus, a less rigid Ge–Ge connectivity.

In addition, a decrease of $\sigma_{\text{Ge–Te}}^2$ in C–GeTe indicates an increase in the rigidity of Ge–Te interactions, possibly due to a more ordered Te sublattice. This is consistent with the observed changes in Ge coordination: in GeTe, most Ge atoms are bonded to two other Ge atoms within Ge chains, causing them to be more localized and with more constrained motion. In C–GeTe, most Ge–Ge bonds are in short Ge chains or dumbbells, meaning the constituent Ge atoms are more likely bonded only to a single other Ge atom on average. These Ge atoms have more positional degrees of freedom, resulting in a greater variance of Ge–Ge bond lengths.

Amorphous GeTe is hypothesized to undergo structural changes prior to crystallization, including a breaking of Ge chains and an increase in the positional ordering of the Te sublattice.[8] To study how C affects these changes, *in situ* FT-EXAFS spectra were analyzed. Qualitatively, the magnitudes of the FT-EXAFS spectra of GeTe and C–GeTe dampen as temperature increases (Fig. 4a and b), which is a well-understood phenomenon attributed to an increase in σ^2 of the scattering paths as temperature and atomic vibrations increase.[8,31–34] As temperature increases, the dynamic disorder of atomic correlations increases. This causes a nearly linear increase in σ^2, which dampens $|\chi(R)|$. Studying how σ^2 changes with temperature is especially valuable since it can separate the

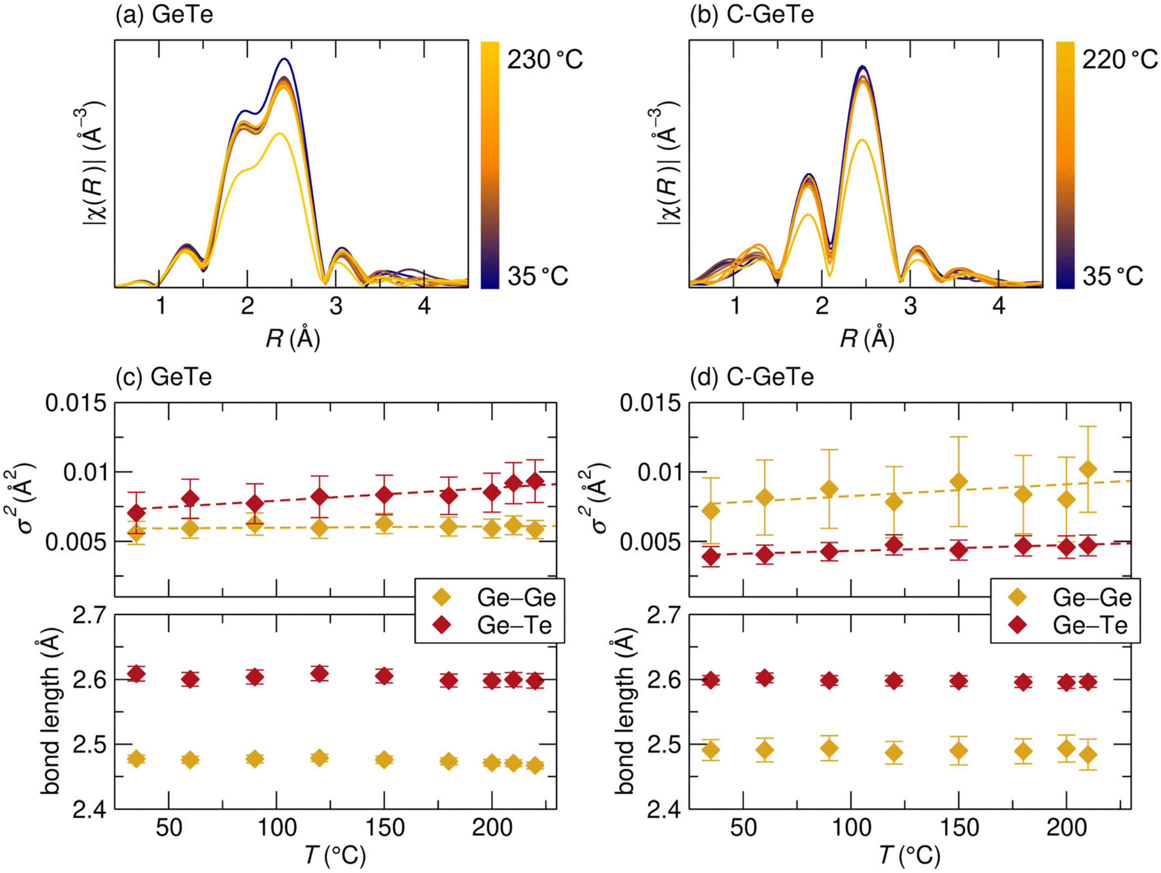

Fig. 4 FT-EXAFS spectra in $|\chi(R)|$ of (a) GeTe and (b) C–GeTe demonstrating signal dampening with increasing temperature. Results of σ^2 and R *versus* temperature from fits to (c) GeTe and (d) C–GeTe *in situ* data. σ^2 values increase linearly as indicated by dotted lines (slopes tabulated in Table 2), but the positions of features in R do not appreciably change.

contributions of dynamic (temperature dependent) and static (temperature independent) disorder.[23,32,33]

While room temperature fits to FT-EXAFS spectra provide a good approximation of the local Ge environment in GeTe and C–GeTe, there is uncertainty regarding the exact values of the fitting parameters. The Ge–Ge and Ge–Te paths overlap in real space and, as a result, the N and σ^2 parameters between and within the paths are correlated. This correlation leads to a significant uncertainty in the fitting parameters, which is underscored by the high standard error for values of N and σ^2 in Table 1. To address this, additional constraints, such as constraining $N_{\text{Ge–Ge}}$ and $N_{\text{Ge–Te}}$ to sum to 4, were applied when fitting. Further, when fitting over the temperature series, $N_{\text{Ge–Ge}}$ and $N_{\text{Ge–Te}}$ were fixed, allowing all changes in scattering path intensities to be represented by changes in σ^2 values. While previous work has indicated that during annealing, Ge–Ge coordination ($N_{\text{Ge–Ge}}$) steadily decreases as long Ge chains break,[8] this effect on $N_{\text{Ge–Ge}}$ is too subtle to quantitatively model in these data given the physical limitations and uncertainty.

Results of the temperature fitting series are shown in Fig. 4c and d and Table 2. A full tabulated version of the *in situ* EXAFS fitting parameters can be found in Tables S1 and S2. GeTe displays expected temperature-dependent behavior, with a roughly linear increase in $\sigma_{\text{Ge–Te}}^2$ with respect to temperature, while $\sigma_{\text{Ge–Ge}}^2$ remains relatively constant. This is due to the higher strength and rigidity of Ge–Ge bonds; the bond length is less susceptible to thermal disorder.[8] In C–GeTe, $\sigma_{\text{Ge–Te}}^2$ increases linearly with increasing temperature, however, with a less steep slope than in GeTe. $\sigma_{\text{Ge–Ge}}^2$ also increases more dramatically with temperature in C–GeTe, indicating a decrease in Ge–Ge bond rigidity with the addition of C.

Table 2 Slopes and goodness-of-fit (R^2) from linear regressions of σ^2 *versus* temperature in amorphous EXAFS fits

Composition	Slope $\sigma_{\text{Ge–Ge}}^2$ ($\text{Å}^2\ {}^\circ\text{C}^{-1} \times 10^{-6}$)	R^2	Slope $\sigma_{\text{Ge–Te}}^2$ ($\text{Å}^2\ {}^\circ\text{C}^{-1} \times 10^{-6}$)	R^2
GeTe	0.9	0.08	9.2	0.80
C–GeTe	8.5	0.35	4.2	0.73

Overall, the results from N, σ^2, and σ^2 *vs.* temperature are aligned with the conceptual model of crystallization in GeTe and the role of C. The addition of C suppresses the formation of Ge–Ge bonds (and thus, Ge chains) as Ge–C bonds form. This decreases the average rigidity of the existing Ge–Ge bonds as Ge atoms move away from tightly bonded covalent chains and closer to their crystalline positions (octahedrally coordinated by Te). Since there are also fewer Ge chains distorting Te atoms from their crystalline positions, that is, an FCC-like sublattice, the Te sublattice also becomes better formed at lower temperatures. In this way, adding C to GeTe causes the amorphous structure to more closely resemble the crystalline phase, rationalizing why C–GeTe has a lower crystallization onset temperature than undoped GeTe.

Here, the structural change observed in both XANES and EXAFS is referred to as 'crystallization onset'. Indeed, the FT-EXAFS spectra after this change show signal representative of scattering paths beyond the first coordination shell, indicating an increase in crystallinity (Fig. S4). Further, rhombohedral GeTe models fit these spectra better than amorphous models (Fig. S5 and Table S3). Yet, these models still require the addition of short Ge–Ge paths to achieve reasonable quality fits, indicating that some Ge_2 dumbbells may persist or bridge adjacent distorted octahedra in this structure (additional information about fitting and fit models are included in the SI). More rigorous diffraction and resistance measurements are needed to fully bridge the crystallization onset behavior observed here with device-relevant crystallization behavior, which is characterized by faster heating and a property measurement (resistance, reflectivity) rather than a structural one.

2.2. X-ray total scattering

In situ X-ray total scattering experiments were conducted for TiN-capped GeTe and C–GeTe films over similar temperature sweeps as *in situ* XAS data. From near room temperature ($\approx$30 °C), samples were heated to a "mid-point" temperature, allowed to passively cool back to room temperature, then heated from room temperature to a maximum near their crystallization onset temperature. The midpoint temperatures were based on the crystallization onset temperatures determined by the first *in situ* XAS experiment (Fig. 2). For GeTe, the mid-point temperature was 176 °C and the maximum temperature was 220 °C, just below its crystallization onset temperature. For C–GeTe, the mid-point temperature was 117 °C and the final temperature was 245 °C. Temperature steps were larger at lower temperature ranges and smaller at higher temperature ranges. Full details of ramp rates and data collection steps are provided in the Experimental Methods section. From the total scattering data, pair distribution functions (PDFs) were derived, from which local- and mid-range atomic structure features and their temperature-dependent behavior were analyzed.

In situ PDFs for GeTe show a slight shift of atomic correlations to lower *r* positions with respect to temperature, as well as an evolution in the shape of some features (Fig. 5a). To highlight changes in the intensities and positions of features in the PDFs during heating and cooling, 'difference PDFs' were calculated by subtracting the initial ambient temperature PDF for each film from all subsequent $G(r)$ data during the first heating and subtracting the second ambient temperature PDF from each film from subsequent PDFs during the second heating (Fig. 5b).

During *in situ* heating, the GeTe film remained amorphous (Fig. S5), but temperature-dependent changes in the position, shape, and intensity of features in the PDFs indicate an evolution of local structure (Fig. 5a). This evidence of local structure evolution before crystallization is consistent with EXAFS analysis, especially regarding changes in Ge motifs and ordering of the Te sublattice.[8]

The first well-defined correlation in the amorphous GeTe PDF is centered near 2.6 Å. In previously proposed models of amorphous GeTe, Ge chains sit within a disordered Te sublattice (Fig. 1a).[8,35] In these models, as in our EXAFS analysis,

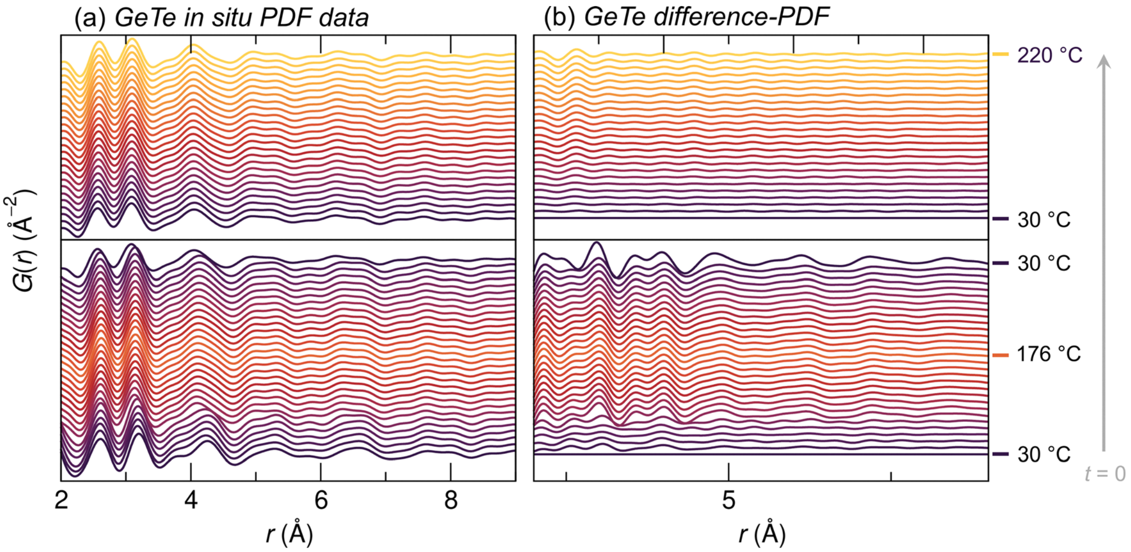

Fig. 5 *In situ* temperature-dependent PDFs for the GeTe film during heating from (bottom panels) 30 °C (t = 0) to 176 °C, then passive cooling to 30 °C; (top panels) and then a second heating to a maximum temperature of 220 °C (below the crystallization onset temperature). (a) PDFs show local structure changes with heating and cooling. To highlight the temperature-dependent feature changes, (b) difference-PDFs were calculated by subtracting the first PDF of each heating stage (30 °C) from subsequent PDFs. Due to a data collection issue, the PDF data at 44 °C, directly before 30 °C, is omitted during the cooling step.

Ge–Ge and Ge–Te bonds are 2.48 Å and 2.61 Å long, respectively (Fig. 1). While these bonds can be distinguished and modeled in EXAFS data, the two bonds cannot be resolved in our X-ray PDF data and instead contribute to a single broad feature centered at 2.6 Å.

In crystalline models of α–GeTe (space group *R*3*m*),[26] the shortest atomic correlations correspond to the short (2.86 Å) and long (3.14 Å) Ge–Te bonds in the distorted [$GeTe_6$] octahedra.[36,37] In our PDFs, the second correlation in the as-deposited amorphous GeTe is at 3.2 Å, similar to the long Ge–Te bond in crystalline GeTe (Fig. 5a). Thus, we attribute the second correlation in the PDF to Ge–Te bonds. Two additional features near 3.8 Å and 4.2 Å are attributed to a network of Te atoms similar to that in an FCC-like sublattice of crystalline GeTe, in which Te atoms are 4.1 Å apart. A simulated PDF of crystalline *R*3*m* GeTe is compared to data collected in this work in Fig. S6.

The first and second features in the GeTe PDF shift to lower *r* upon heating, distinct from what would be expected from thermal expansion or thermally-driven (dynamic) atomic vibrations. The first feature (≈2.6 Å), attributed to a combination of Ge–Ge and Ge–Te bonds in the amorphous structure, approaches the Ge–Ge bond length determined from EXAFS analysis at similar temperatures (2.48 Å). The second feature (≈3.2 Å), primarily associated with Ge–Te correlations, moves toward the average of the Ge–Te bond lengths in the crystalline structure. The shift in position is continuous during early heating, and then changes abruptly at ≈103 °C (Fig. 5a). This change in the feature's position is highlighted by the 'heartbeat' motif at the corresponding *r* position in the difference-PDF data (Fig. 5b). Overall, during the first heating to the midpoint temperature of 176 °C, the first and second correlations moves from 2.6 Å to 2.5 Å and 3.2 Å to 3.0 Å, respectively.

The features initially at 3.8 Å and 4.2 Å in GeTe data also change during the first heating, appearing to merge into one feature centered at ≈4.1 Å. The evolution of features in this *r* range is dominated by the shift of the 4.2 Å feature to lower *r* (Fig. 5). We interpret the shift in position as the Te sublattice of the crystalline structure beginning to arrange before crystallization, as has been previously reported for models of the crystallization mechanism of GeTe.[8]

Higher *r* features in PDF have less intensity than lower *r* features, as expected for an amorphous material without long-range order. During the first heating, changes in these higher *r* features are subtle relative to the changes at lower *r*. As a result of the small initial amplitude of these features and the persistence of long-range disorder, it is difficult to distinguish changes of higher *r* correlations and likewise to attribute them to specific structural motifs (Fig. 5).

After reaching the midpoint temperature for GeTe during the first heating (176 °C), the film was allowed to passively cool back to ambient temperature. During cooling, the PDF features revert towards those of the original ambient temperature PDF, but do not fully return to the as-deposited state; some features change more reversibly than others. The feature originally at 3.8 Å, which merged with a higher *r* feature during the first heating, re-emerges upon cooling from the midpoint temperature. Likewise, higher *r* features that became more well-defined during the first heating lose some definition during cooling. In contrast, the changes in position of the first two features persist upon cooling from the midpoint temperature. The reversion is evident in the PDF data directly, and further highlighted in the difference PDF data from the first heating and cooling step, which shows a decrease in intensity during cooling (Fig. 5b, bottom panel).

During the second heating, the positions and intensities of PDF features in GeTe continue to evolve (Fig. 5, top panel). The first feature, initially centered at 2.6 Å, shifts to lower *r* during the second heating; at the maximum temperature of 220 °C, the feature is centered above 2.5 Å. Similarly, the second feature, initially centered at 3.2 Å continues to shift to lower *r* during the second heating step. The broad feature centered near 4.2 Å shifts to slightly lower *r*, following the same trend of the first heating. The feature remains just over 4.0 Å during the second heating, near the Te–Te correlation distances of crystalline α–GeTe. This feature also narrows with increasing temperature. The evolution of a broad feature to a narrower one indicates that there is decreasing variability in the distribution of atom-atom pair distances contributing to this feature, reflective of increased ordering in the Te sublattice. This anion sublattice ordering is consistent with proposed pre-crystallization structural evolution.[8]

Features at higher *r* show subtle changes on the second heating compared to the lower *r* features. These high *r* features do not show evidence of an amorphous-to-crystalline phase transformation, in which more well defined features at higher *r* would become evident with long-range order.

We interpret the observed changes in the context of previously proposed models of crystallization for GeTe. In the mechanism proposed by Wintersteller *et al.*,[8] based on molecular dynamics simulations and XAS measurements, the structure of amorphous GeTe evolves with Ge chains breaking into shorter chains, dumbbells, or individual atoms while the Te sublattice orders, even before crystallization. This process continues to form the fully crystallized atomic structure, with any remaining chains breaking and Ge atoms positionally ordering into an octahedral coordination.

Overall, there are pronounced structural shifts in low *r* during the first heating and cooling and subtle, continued structural evolution during the second heating. At the end of the second heating, though the film remains amorphous, the change in PDF features indicates pre-crystallization evolution that is consistent with the proposed model of GeTe crystallization.

In situ PDFs for doped C–GeTe (Fig. 6) show a lesser degree of structural change compared to GeTe across similar temperature ranges (Fig. 6). This is consistent through both heating stages, even as the second heating extends to higher temperatures. The relative stability of local- and mid-range atomic structure features in PDFs for C–GeTe are also consistent with our *in situ* EXAFS data, which show less change in the Ge local environment for C–GeTe than GeTe.

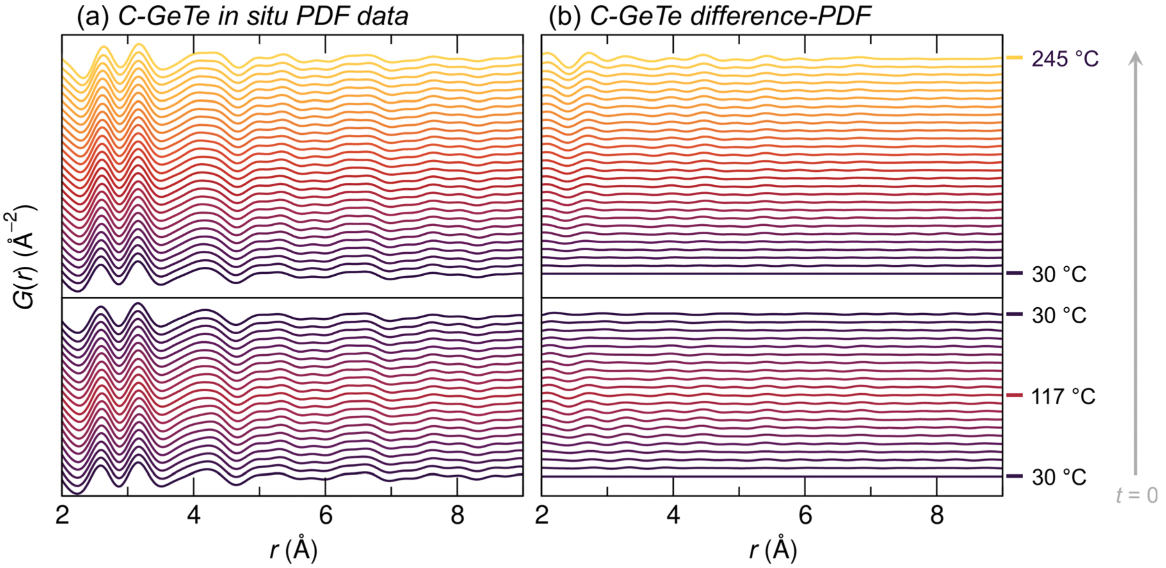

Fig. 6 *In situ* temperature-dependent PDFs for the C–GeTe film during heating (bottom panels) from 30 °C (*t* = 0) to 117 °C, then passive cooling to 30 °C; (top panels) and a second heating to a maximum temperature of 245 °C (above the crystallization onset temperature of 220 °C). (a) PDFs show local structure changes with heating and cooling. To highlight the temperature-dependent feature changes and reversibility, (b) difference-PDFs were calculated by subtracting the first PDF of each heating stage (30 °C) from subsequent PDFs.

During the first heating of the C–GeTe film, there are no obvious changes in the PDF data (Fig. 6, bottom panels), even for the low *r* correlations that evolved appreciably in the GeTe film at comparable temperatures. However, the difference-PDF does indicate minor, continuous, and reversible changes during the first heating and cooling. The changes are most pronounced at low *r*, especially for the feature centered near 2.6 Å in the as-deposited state. The center of the intensity of this feature moves to higher *r* with heating, but reverses upon cooling.

During the second heating, the evolution of features follows a similar path as the first, continuing the subtle trends seen in the first heating and extending through higher temperatures (Fig. 6, top panels). This includes the same shift of the first correlation (2.6 Å in the as-deposited film) to higher *r*. The heartbeat motif in the difference-PDF, indicating an increase in *r* position, is more prominent during the second heating step (Fig. 6b, top panel). Other features in the C–GeTe PDF show small magnitudes of change as temperature increases through the second heat.

As for GeTe, the PDFs for C–GeTe at the maximum temperature do not show evidence of long-range order, even with data collected slightly above the crystallization onset temperature identified in XANES. The total scattering data collected at this temperature show broad, low-intensity Bragg peaks (Fig. S8), however, the bulk of the sample remains amorphous at the time and temperature conditions of the PDF measurement.

3. Further discussion

In previous reports, the atomic structure of amorphous GeTe is described as comprising a disordered Te sublattice infiltrated with Ge as individual atoms, dumbbell pairs, and polymer-like chains (Fig. 1a). During heating, the Te sublattice becomes more ordered and long Ge chains break down into shorter Ge chains, eventually forming long-range crystalline order (Fig. 1).

Using complementary *in situ* local structure characterization, we identify differences in the as-deposited amorphous structure of GeTe and C-doped GeTe, as well as the evolution of the atomic structures in response to temperature changes. From EXAFS analysis, we find that incorporating C modifies the amorphous GeTe structure such that its as-deposited state is closer to the state of the crystalline model than in undoped GeTe. The as-deposited PDF data have less-defined features, especially at medium-range (5 Å to 8 Å) and higher *r*. We propose a model for amorphous C–GeTe in which C disrupts Ge–Ge bonding, resulting in Ge chains that are shorter and a Te sublattice that is closer to its FCC-like configuration than in undoped GeTe. The proposed change in Ge bonding behavior is reflected in EXAFS analysis by the decreased coordination of Ge by Ge and decreased rigidity of Ge–Ge bonds, consistent with Ge in shorter chains with less constrained dynamic atomic motion. A similar tendency for C to replace some Ge–Ge bonds in amorphous chalcogenides has been reported for phase-change material $Ge_2Sb_2Te_5$ and related compounds.[12,23,24,27,38]

With C interrupting Ge chains in the as-deposited structure, less chain scission is required for the material to crystallize, leading to a lower crystallization onset temperature for the C–GeTe film relative to GeTe. The lower crystallization onset temperature of C–GeTe that we identify through *in situ* XANES, 220 °C in C–GeTe *vs.* 230 °C in GeTe, is supported by local structure differences in the as-deposited C–GeTe film. Yet, the lack of diffraction peaks in total scattering data at this temperature, and the lack of complementary resistivity measurements, leaves this so-called 'crystallization onset' behavior and definitive crystallization as-yet uncoupled.

In related PCMs, such as $Ge_2Sb_2Te_5$, C dopants have the opposite effect on the crystallization onset temperature, increasing the amorphous-to-crystalline transformation temperature, as well as the cubic-to-monoclinic transition at higher temperatures.[22–24,27] Although C–GeTe total scattering data (Fig. S8) above 220 °C shows some broad, low intensity peaks as evidence of a more crystalline structure, this change in ordering is not reflected in the PDF data at corresponding temperatures. Given that GeTe follows a nucleation and growth model of crystallization,[39,40] crystalline regions may be nanoscale domains and comprise a minority of the volume of the C–GeTe film with the majority of the sample remaining amorphous, consistent with high-temperature PDF data.

Crystallization temperature in GeTe is formally defined by a sharp drop in resistivity of a film or device as temperature is increased.[7,9,11,24] Such resistance-temperature measurements are quick, which is relevant for the fast time scales of crystallization and amorphization in a device. However, our XAS and PDF measurements are slower, with data collected over 30 and 2 minutes, respectively, per temperature increment. GeTe and C–GeTe films are known to structurally relax (*i.e.*, crystallize) at an elevated temperature below T_C after an extended period of time. Betti Beneventi *et al.* found that the addition of 4 at% C into GeTe increased T_C from 180 °C to 290 °C, as measured by reflectivity and resistance measurements. Yet, when both films (as devices) were annealed at 170 °C, below T_C, GeTe crystallized over the course of seconds, and C–GeTe crystallized over the course of minutes.[14] In other words, the crystallization onset behavior of the two films was similar to our own films, in which both of the films crystallized over the course of minutes at temperatures near to each other (and likely below T_C). Similar behavior occurred in the work by Wintersteller *et al.*, where GeTe annealed at a temperature below T_C crystallized after 30 minutes.[8]

Overall, we do not seek to refute established trends between C content and T_C in GeTe. Instead, we characterize the short- and medium-range structure effect of C on GeTe at low concentrations that impacts the crystallization onset mechanism during anneals at elevated temperature. This is especially relevant for the processing of C–GeTe devices, in which extended anneals may occur, or the incorporation of C–GeTe devices in high-temperature environments. Further work including resistance- or reflectivity-temperature measurements, Raman spectroscopy, and supplementary computational studies would be necessary to fully understand the relationship between this phenomenon and T_C in C–GeTe, as well as directly characterize the role of C in the structure.

4. Conclusions

Complementary EXAFS and PDF analyses reveal temperature- and composition-dependent structure–property relationships in GeTe thin films. Specifically, we find that C dopants modify the as-deposited structure of GeTe films by changing the extent of Ge–Ge bonds in the amorphous state, increasing the population of lone Ge or Ge dumbbells rather than longer Ge chains. This has an effect on crystallization onset behavior during extended anneal times on the order of minutes.

We also further establish a promising application of a novel technique, thin-film PDF. Zhou *et al.* found differences in the crystallization temperature of GeTe films based on thickness, suggesting that the crystallization behavior is influenced by morphology.[7] As PDF methods for thin films mature, studying films with a variety of thicknesses, substrates, and capping layers may provide much-needed insights regarding the origins of structure and function in phase-change material thin films.[41–45]

5. Experimental methods

5.1. Synthesis

GeTe and $(GeTe)_{0.96}C_{0.04}$ (C–GeTe) films were synthesized by direct current magnetron sputter deposition using a Unifim Co. PVD-300 system using targets from Process Materials, Inc. The 300 nm thick films were deposited onto 500 μm thick silica substrates with 30 nm TiN capping layers. Preceding deposition, the chamber was evacuated to an initial pressure of 5×10^{-7} Torr. For sputtering, ultrahigh purity argon gas (99.999%) was used as a sputtering gas, maintained at 10 mTorr while the chamber was maintained at 60 °C.

5.2. X-ray absorption spectroscopy

XAS measurements were collected at the Beamline for Materials Measurement (6-BM) at the National Synchrotron Lightsource-II (NSLS-II) at Brookhaven National Laboratory. Measurements were made from 200 eV below the Ge K-edge (11 103 eV) to 650 eV past the edge in fluorescence mode. Linkam cells were used for *in situ* data collection during heating in air. Spectra were collected at varying increments from room temperature to the crystallization temperature, with more dense increments near the crystallization temperature. After a 1 minute dwell period at the set temperature, three consecutive scans were taken for statistical averaging.

XAS data reduction was performed using Larix/Larch.[30] Normalized spectra were weighted using a k weighting of 2.0, background subtraction with a R_{bkg} value of 1.30, and a k window from 2.00 Å^{-1} to 12.00 Å^{-1}. Resulting spectra were Fourier transformed using a Hanning window and a k range of 2.00 Å^{-1} to 11.00 Å^{-1}.

EXAFS fitting was performed using Larix/Larch.[30] To generate the amorphous Ge–Ge and Ge–Te paths, the potential of a modified structure of rhombohedral ($R3m$) GeTe was calculated using feff in Larix.[25] In the nominal GeTe structure, each Ge atom is coordinated by Te in 3 short (2.84 Å) and 3 long (3.16 Å) Ge–Te bonds. In the modified structure, one Te atom at the shorter distance was replaced with Ge to calculate the Ge–Ge path in the modified structure. Further, the a and c lattice parameters were decreased by 10% so that the starting Ge–Ge and Ge–Te half-path lengths were reduced to 2.55 Å, closer to the known bond distances in amorphous GeTe.

Models were fit to FT-EXAFS spectra from 1.4 Å to 3 Å in real space with a k weighting of 2. N values were constrained to be positive and sum to 4. σ^2 values were constrained between 0.001 $Å^2$ and 0.02 $Å^2$. R values were constrained to not exceed a 0.10 Å difference from the original starting value (2.47 Å for Ge–Ge, 2.63 Å for Ge–Te). An initial fit for GeTe was made with $S_0{}^2$ unconstrained. The resulting value of $S_0{}^2 = 0.79$ was applied for all subsequent fits and constrained to be constant to reduce correlation effects of $S_0{}^2$ and N.[46]

Additional spectra, analysis, and fitting information are provided in the SI.

5.3. X-ray scattering data collection

X-ray scattering data were collected at the Pair Distribution Function beamline (28-ID-1) at National Synchrotron Light Source II at Brookhaven National Laboratory. Data were collected at a sample-to-detector distances of 21.9 cm to acquire X-ray total scattering to high Q to access local- and mid-range atomic structure information from PDF data. X-rays had a wavelength of 0.1665 Å (74.465 keV) and scattered data were collected using a PerkinElmer Si detector. A modified Linkam cell was used for *in situ* data collection during heating in air. To enable X-ray transmission, holes were drilled in both sides of the Linkam cell. This resulted in a systematic discrepancy between the set and actual temperature, thus the collected temperature points for *in situ* X-ray scattering data are inaccurate, but the trend of temperature between GeTe and C–GeTe films holds. Due to this, the temperature values assigned to X-ray scattering and PDF data were based on the known crystallization temperature for each composition obtained through XANES measurements and scaled accordingly.

5.4. X-ray scattering and PDF data processing

A custom python package, ProcessDAT (https://github.com/ButalaResearchGroup/ProcessDAT), was used to process the raw 2D X-ray total scattering data. ProcessDAT automates some of the processing of series of related data. ProcessDAT uses an application programming interface (API) of PyFAI to integrate 2D scattering patterns to 1D data.[47] The instrument parameters were determined using a Ni calibrant, including separate parameters for the two sample-to-detector distances.

ProcessDAT was also to automate the subtraction of a background; in this case, the background was the 1D scattering data from an amorphous SiO_2 substrate with no film. Conventionally, subtracting the substrate data requires manually scaling the intensity to maximize background removal without oversubtracting and introducing artefacts.[41,42] With ProcessDAT, the scaling and subtraction steps are combined and automated to batch process large dataset, such as time or temperature series, which can have fluctuating intensities due to beam intensity variations during data collection.

The isolated scattering data from the thin films were then processed into $G(r)$ data using PDFgetX3.[48] We used parameters: $q_{\min} = 2.5\ Å^{-1}$, $q_{\max} = 14\ Å^{-1}$, and $r_{\text{poly}} = 1.0$ to process total scattering data to PDFs. PDF data were scaled and displayed in waterfall plots with offsets to highlight relationships between features over the temperature series.

Author contributions

JDL: conceptualization, data curation, formal analysis, investigation, methodology, validation, visualization, writing – original draft, writing – review & editing. MDK: conceptualization, data curation, formal analysis, methodology, software, validation, visualization, writing – original draft, writing – review & editing. DNA: conceptualization, data curation, formal analysis, investigation, methodology, software. LB: software. CM: software. DO: investigation, methodology, software. DPA: conceptualization, funding acquisition, project administration, resources. MMB: conceptualization, funding acquisition, methodology, project administration, resources, supervision, visualization, writing – original draft, writing – review & editing.

Conflicts of interest

There are no conflicts to declare.

Data availability

All X-ray absorption spectroscopy data in the form of normalized X-ray absorption near-edge structure (XANES) spectra and Fourier-transformed extended X-ray absorption fine structure (FTEXAFS) spectra are included in the main manuscript and the supplemental materials. All total scattering data (1D integrations, and Fourier-transformed pair distribution functions) are included in the main manuscript and the supplemental materials. Additionally, 1D integrations from total scattering data are included, as data files, in the GitHub repository below. The code used to process total scattering data in this work (''ProcessDAT'') can be found at the following GitHub repository: D. Alverson, L. Barnes, M. Kelley, C. Mercier, 2026, ButalaResearchGroup/ProcessDAT, https://github.com/ButalaResearchGroup/ProcessDAT.

Supplementary information (SI) is available. See DOI: https://doi.org/10.1039/d6tc01061j.

Acknowledgements

The authors thank Bruce Ravel for support with X-ray absorption spectroscopy measurements and John Trunk for support with *in situ* measurement setup. This research utilized the Beamline for Materials Measurement (BMM, 6-BM) and the Pair-Distribution Function (PDF, 28-ID-1) beamline of the National Synchrotron Light Source II, a U.S. Department of Energy (DOE) Office of Science User Facility operated for the DOE Office of Science by Brookhaven National Laboratory under Contract No. DE-SC0012704. This work was supported by the Sandia National Laboratory Directed Research and Development (LDRD) program. Sandia National Laboratories is a multi-mission laboratory managed and operated by National Technology and Engineering Solutions of Sandia, LLC. (NTESS), a wholly owned subsidiary of Honeywell International, Inc., for the U.S. Department of Energy's National Nuclear Security Administration (DOE/NNSA) under Contract No. DE-NA0003525. This written work is authored by an employee of NTESS. The employee, not NTESS, owns the right, title, and interest in and to the written work and is responsible for its contents. This work describes objective technical results and analysis. Any subjective views or opinions that might be expressed in the paper do not necessarily represent the views of the U.S. Department of Energy or the U.S. Government. The publisher acknowledges that the U.S. Government retains a non-exclusive, paid-up, irrevocable, world-wide license to publish or reproduce the published form of this written work or allow others to do so, for U.S. Government purposes. The DOE will provide public access to results of federally sponsored research in accordance with the DOE Public Access Plan.

References

1 M. L. Gallo and A. Sebastian, An overview of phase-change memory device physics, *J. Phys. D: Appl. Phys.*, 2020, **53**, 213002.

2 M. Wuttig and S. Raoux, The Science and Technology of Phase Change Materials, *Z. Anorg. Allg. Chem.*, 2012, **638**, 2455–2465.

3 P. Guo, A. Sarangan and I. Agha, A Review of Germanium-Antimony-Telluride Phase Change Materials for Non-Volatile Memories and Optical Modulators, *Appl. Sci.*, 2019, **9**, 530.

4 P. Noé, A. Verdy, F. d'Acapito, J.-B. Dory, M. Bernard, G. Navarro, J.-B. Jager, J. Gaudin and J.-Y. Raty, Toward ultimate nonvolatile resistive memories: The mechanism behind ovonic threshold switching revealed, *Sci. Adv.*, 2020, **6**, eaay2830, DOI: 10.1126/sciadv.aay2830.

5 Y. Ren, R. Sun, S. H. Y. Chen, C. Du, S.-T. Han and Y. Zhou, Exploring Phase-Change Memory: From Material Systems to Device Physics, *Phys. Status Solidi RRL*, 2021, **15**, 2000394.

6 J. Keukelier, K. Opsomer, T. Nuytten, S. Sergeant, W. Devulder, S. Clima, L. Goux, G. S. Kar and C. Detavernier, Impact of changes in bond structure on ovonic threshold switching behaviour in $GeSe_2$, *J. Mater. Chem. C*, 2021, **9**, 117–126.

7 Z. Zhou, W. Wu, Y. Li and J. Zhai, Thickness dependence and crystallization properties of amorphous GeTe thin films on silicon dioxide, *Phys. Scripta*, 2024, **99**, 105980.

8 S. Wintersteller, O. Yarema, D. Kumaar, F. M. Schenk, O. V. Safonova, P. M. Abdala, V. Wood and M. Yarema, Unravelling the amorphous structure and crystallization mechanism of GeTe phase change memory materials, *Nat. Commun.*, 2024, **15**, 1011.

9 T. Gwon, A. Y. Mohamed, C. Yoo, E.-S. Park, S. Kim, S. Yoo, H.-K. Lee, D.-Y. Cho and C. S. Hwang, Structural Analyses of Phase Stability in Amorphous and Partially Crystallized Ge-Rich GeTe Films Prepared by Atomic Layer Deposition, *ACS Appl. Mater. Interfaces*, 2017, **9**, 41387–41396.

10 C. Y. Khoo, H. Liu, W. A. Sasangka, R. I. Made, N. Tamura, M. Kunz, A. S. Budiman, C. L. Gan and C. V. Thompson, Impact of deposition conditions on the crystallization kinetics of amorphous GeTe films, *J. Mater. Sci.*, 2016, **51**, 1864–1872.

11 Y. G. Choi, S. Y. Shin, R. Golovchak, B.-K. Cheong and H. Jain, Comparative study of atomic arrangements in equiatomic GeSe and GeTe films before and after crystallization, *J. Alloys Compd.*, 2016, **686**, 273–280.

12 G. E. Ghezzi, J. Y. Raty, S. Maitrejean, A. Roule, E. Elkaim and F. Hippert, Effect of carbon doping on the structure of amorphous GeTe phase change material, *Appl. Phys. Lett.*, 2011, **99**, 151906.

13 X. Biquard, M. Krbal, A. V. Kolobov, P. Fons, R. E. Simpson, B. Hyot, B. André, J. Tominaga and T. Uruga, Effect of doping on global and local order in crystalline GeTe, *Appl. Phys. Lett.*, 2011, **98**, 231907.

14 G. Betti Beneventi, *et al.*, Carbon-doped GeTe: A promising material for Phase-Change Memories, *Solid-State Electron.*, 2011, **65–66**, 197–204.

15 Y. M. Yoshihito Maeda and M. W. Masatoshi Wakagi, Ge K-Edge Extended X-Ray Absorption Fine Structure Study of the Local Structure of Amorphous GeTe and the Crystallization, *Jpn. J. Appl. Phys.*, 1991, **30**, 101.

16 K. Ohara, L. Temleitner, K. Sugimoto, S. Kohara, T. Matsunaga, L. Pusztai, M. Itou, H. Ohsumi, R. Kojima, N. Yamada, T. Usuki, A. Fujiwara and M. Takata, The Roles of the Ge-Te Core Network and the Sb-Te Pseudo Network During Rapid Nucleation-Dominated Crystallization of Amorphous $Ge_2Sb_2Te_5$, *Adv. Funct. Mater.*, 2012, **22**, 2251–2257.

17 H. K. Seo, J. J. Ryu, S. Y. Lee, M. Park, S. Park, W. Song, G. H. Kim and M. K. Yang, Material and Structural Engineering of Ovonic Threshold Switch for Highly Reliable Performance, *Adv. Electron. Mater.*, 2022, **8**, 2200161.

18 L. Wang, W. Cai, D. He, Q. Lin, D. Wan, H. Tong and X. Miao, Performance Improvement of $GeTe_x$-Based Ovonic Threshold Switching Selector by C Doping, *IEEE Electron Device Lett.*, 2021, **42**, 688–691.

19 D. Seong, S. Y. Lee, H. K. Seo, J.-W. Kim, M. Park and M. K. Yang, Highly Reliable Ovonic Threshold Switch with TiN/GeTe/TiN Structure, *Mater*, 2023, **16**, 2066.

20 S. R. Ovshinsky, Reversible Electrical Switching Phenomena in Disordered Structures, *Phys. Rev. Lett.*, 1968, **21**, 1450–1453.

21 J.-Y. Raty, P. Noé, G. Ghezzi, S. Maıtrejean, C. Bichara and F. Hippert, Vibrational properties and stabilization mechanism of the amorphous phase of doped GeTe, *Phys. Rev. B: Condens. Matter Mater. Phys.*, 2013, **88**, 014203.

22 E. A. Scott, E. Ziade, C. B. Saltonstall, A. E. McDonald, M. A. Rodriguez, P. E. Hopkins, T. E. Beechem and D. P. Adams, Thermal conductivity of $(Ge_2Sb_2Te_5)_{1-x}C_x$ phase change films, *J. Appl. Phys.*, 2020, **128**, 155106.

23 J. D. Langhout, D. N. Alverson, C. Ginter, B. Ravel, D. P. Adams and M. M. Butala, Local structure effects of carbon-

doping on the phase change material $Ge_2Sb_2Te_5$, *J. Mater. Chem. C*, 2024, **12**(22), 7867–7877.

24 H. Hu, S. Yuan, S. Tang, Q. Xu, M. Xu, Q. He, H. Tong, S. Wang, C.-Z. Wang and X. Miao, *et al.*, Engineering neuromorphic phase-change memory: Carbon-doped GeSbTe with high thermal stability and low resistance drift, *Appl. Phys. Lett.*, 2026, 128.

25 M. Samanta, T. Ghosh, R. Arora, U. V. Waghmare and K. Biswas, Realization of Both n- and p-Type GeTe Thermoelectrics: Electronic Structure Modulation by $AgBiSe_2$ Alloying, *J. Am. Chem. Soc.*, 2019, **141**, 19505–19512.

26 T. Nonaka, G. Ohbayashi, Y. Toriumi, Y. Mori and H. Hashimoto, Crystal structure of GeTe and $Ge_2Sb_2Te_5$ meta-stable phase, *Thin Solid Films*, 2000, **370**, 258–261.

27 T. Li, L. Wu, X. Ji, Y. Zheng, G. Liu, Z. Song, J. Shi, M. Zhu, S. Song and S. Feng, Carbon doping induced Ge local structure change in as-deposited $Ge_2Sb_2Te_5$ film by EXAFS and Raman spectrum, *AIP Adv.*, 2018, **8**, 025201.

28 A.-K. U. Michel, M. Sousa, M. Yarema, O. Yarema, V. Ovuka, N. Lassaline, V. Wood and D. J. Norris, Optical Properties of Amorphous and Crystalline GeTe Nanoparticle Thin Films: A Phase-Change Material for Tunable Photonics, *Am. Chem. Soc. Appl. Nano Mater.*, 2020, **3**, 4314–4320.

29 A. Velea, C. N. Borca, G. Socol, A. C. Galca, D. Grolimund, M. Popescu and J. A. van Bokhoven, In-situ crystallization of GeTe\GaSb phase change memory stacked films, *J. Appl. Phys.*, 2014, **116**, 234306.

30 M. Newville, Larch: An Analysis Package for XAFS and Related Spectroscopies, *J. Phys.: Conf. Ser.*, 2013, **430**, 012007.

31 N. Abd el All, B. Thiodjio Sendja, R. Grisenti, F. Rocca, D. Diop, O. Mathon, S. Pascarelli and P. Fornasini, Accuracy evaluation in temperature-dependent EXAFS measurements of CdTe, *J. Synchrotron Radiat.*, 2013, **20**, 603–613.

32 P. Fornasini and R. Grisenti, On EXAFS Debye-Waller factor and recent advances, *J. Synchrotron Radiat.*, 2015, **22**, 1242–1257.

33 P. P. Lottici, G. Antonioli and C. Razzetti, Bond strengths in defect chalcopyrite $ZnGa_2Se_4$ by temperature dependence of EXAFS, *J. Phys. Chem. Solids*, 1988, **49**, 1057–1061.

34 W. Bohmer and P. Rabe, Temperature dependence of the mean square relative displacements of nearest-neighbour atoms derived from EXAFS spectra, *J. Phys. C: Solid State Phys.*, 1979, **12**, 2465–2474.

35 V. L. Deringer, W. Zhang, M. Lumeij, S. Maintz, M. Wuttig, R. Mazzarello and R. Dronskowski, Bonding Nature of Local Structural Motifs in Amorphous GeTe, *Angew. Chem., Int. Ed.*, 2014, **53**, 10817–10820.

36 T. Chatterji, S. Rols and U. D. Wdowik, Dynamics of the phase-change material GeTe across the structural phase transition, *Front. Phys.*, 2018, **14**, 23601.

37 K. Jeong, S. Park, D. Park, M. Ahn, J. Han, W. Yang, H.-S. Jeong and M.-H. Cho, Evolution of crystal structures in GeTe during phase transition, *Sci. Rep.*, 2017, **7**, 955.

38 X. Zhou, M. Xia, F. Rao, L. Wu, X. Li, Z. Song, S. Feng and H. Sun, Understanding Phase-Change Behaviors of Carbon-Doped $Ge_2Sb_2Te_5$ for Phase-Change Memory Application, *ACS Appl. Mater. Interfaces*, 2014, **6**, 14207–14214.

39 B. Croes, F. Cheynis, Y. Fagot-Revurat, P. Müller, S. Curiotto and F. Leroy, Early-stage growth of GeTe on Si(111)-Sb, *Phys. Rev. Mater.*, 2023, **7**, 014409.

40 M. J. Müller, C. Morell, P. Kerres, M. Raghuwanshi, R. Pfeiffer, S. Meyer, C. Stenz, J. Wang, D. N. Chigrin, P. Lucas and M. Wuttig, Decoupling Nucleation and Growth in Fast Crystallization of Phase Change Materials, *Adv. Funct. Mater.*, 2024, **34**, 2403476.

41 K. M. Ø. Jensen, A. B. Blichfeld, S. R. Bauers, S. R. Wood, E. Dooryhée, D. C. Johnson, B. B. Iversen and S. J. L. Billinge, Demonstration of thin film pair distribution function analysis (tfPDF) for the study of local structure in amorphous and crystalline thin films, *IUCrJ*, 2015, **2**, 481–489.

42 A.-C. Dippel, O. Gutowski, L. Klemeyer, U. Boettger, F. Berg, T. Schneller, A. Hardtdegen, S. Aussen, S. Hoffmann-Eifert and M. V. Zimmermann, Evolution of shortrange order in chemically and physically grown thin film bilayer structures for electronic applications, *Nanoscale*, 2020, **12**, 13103–13112.

43 D. N. Alverson, D. Olds and M. M. Butala, Distinguishing isotropic and anisotropic signals for X-ray total scattering using machine learning, *Acta Crystallogr. A*, 2025, **81**, 175–187.

44 M. I. Büschges, V. Trouillet, A.-C. Dippel and J. J. Schneider, Amorphous Doped Indium Tin Oxide Thin-Films by Atomic Layer Deposition. Insights into Their Structural, Electronic and Device Reliability, *Adv. Mater. Interfaces*, 2025, **12**, 2400758.

45 M. I. Büschges, C. Dietz, V. Trouillet, A.-C. Dippel, F. Igoa Saldana and J. J. Schneider, Precise Tailoring of Charge Transport Characteristics in Zr and Hf Doped Indium Tin Oxide Thin Film Transistors, *Adv. Electron. Mater.*, 2026, e00722.

46 B. Ravel and S. D. Kelly, The Difficult Chore of Measuring Coordination by EXAFS, *AIP Conference Proceedings*, Stanford, California (USA), 2007, 150–152.

47 G. Ashiotis, A. Deschildre, Z. Nawaz, J. P. Wright, D. Karkoulis, F. E. Picca and J. Kieffer, The fast azimuthal integration Python library: *pyFAI*, *J. Appl. Crystallogr.*, 2015, **48**, 510–519.

48 P. Juhás, T. Davis, C. L. Farrow and S. J. Billinge, PDFgetX3: a rapid and highly automatable program for processing powder diffraction data into total scattering pair distribution functions, *J. Appl. Crystallogr.*, 2013, **46**, 560–566.